Bidirectional Isolated Half Bridge Three-Level Resonant DC–DC Converter and Optimized Modulation Strategy

Guangfu Hu, Fengjiang Wu, *Senior Member, IEEE*, and Yongfeng Qin

***Abstract*—In this article, a bidirectional isolated half-bridge three-level resonant dc–dc converter is proposed, where the voltage stresses of all power switches are limited to half of the input or output voltage. Only eight power switches are used in the proposed converter and the system volume and cost are decreased. The corresponding universal modulation strategy with the ability of auto-balance of the dc side split capacitors voltages is proposed and the steady-state characteristics is analyzed. In order to improve the efficiency, a multivariable coordinated optimization modulation strategy is proposed to realize the full-range quasi-minimum current trajectory and the full range zero voltage switching. The switching loss, conducting loss, and current stress are all reduced. The correctness and feasibility of the proposed converter and its optimization modulation strategy are verified by the detailed experiment results.**

***Index Terms*—DC–DC converter, half-bridge three-level (HBTL), optimization modulation strategy.**

I. Introduction

In RECENT years, the bidirectional isolated dc–dc converters have demonstrated advantages such as the excellent isolation performance, high power density, bidirectional power transfer, and high efficiency. The converter has broad prospects in the fields of the dc distribution systems, energy storage systems, electric vehicles, and renewable energy generation [1], [2], [3]. The higher power density and efficiency are the important development trends for this converter [4], [5].

In the low-voltage applications, many researches on the dual active bridge (DAB) converter have been made in the aspects of topology, modulation strategies, closed-loop control, etc. [6], [7]. In the middle voltage application, in order to reduce the voltage stress, a common approach is to connect multiple DAB modules in series or parallel. However, the numerous DAB modules increase the number of transformers and the control complexity [8]. The volume and cost are increased. Therefore, in order to reduce the number of modules needed and utilize the power switches with lower rated voltages, the multilevel circuits are widely used for the middle-voltage dc–dc power conversion.

Received 18 May 2025; revised 15 July 2025; accepted 7 August 2025. Date of publication 13 August 2025; date of current version 23 December 2025. Recommended for publication by Associate Editor M. Ponce-Silva. *(Corresponding author: Fengjiang Wu.)*

The authors are with the School of Electrical Engineering, Harbin Institute of Technology, Harbin 150001, China (e-mail: shimeng@hit.edu.cn).

Color versions of one or more figures in this article are available at https://doi.org/10.1109/TPEL.2025.3598084.

Digital Object Identifier 10.1109/TPEL.2025.3598084

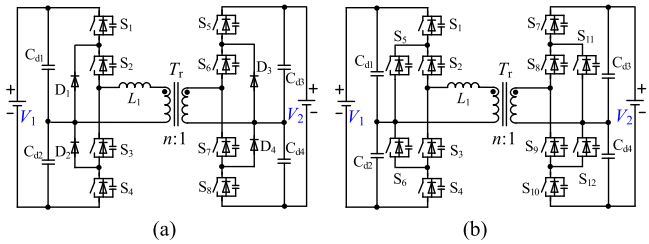

Fig. 1. Bidirectional isolated TL DC–DC converters. (a) DNPC-DAB. (b) ANPC-DAB.

Currently, the three-level (TL) dc–dc converters are the most widely applied among the multilevel converters. The main types include T-type [9], diode neutral point clamped (DNPC) [10], [11], [12], [13], flying capacitor [14], hybrid neutral point clamped (HNPC) [8], [15], [16], [17], [18], active neutral point clamped (ANPC) [19], [20], [21] and half-bridge three-level (HBTL) [22], [23], [24], [25], [26], [27] converters.

The DNPC-DAB converter is shown in Fig. 1(a). Since the lack of the redundant switching states in DNPC leads to the unbalanced distribution of power losses, the ratings of the power switches and heat sink are increased. In addition, the switching losses are significantly increased by the long commutation loop. The unreliable clamping and the unbalanced distribution of power losses in the DNPC-DAB converter are solved by employing the flying capacitor or hybrid clamping methods [14], [15], [16], [17], [18]. However, the balance of the flying capacitor voltage is complex, and the reliability and practicality are reduced. Compared to DNPC, in order to achieve the reliable voltage clamping and the redundant zero switching states, the clamping diodes are replaced by the power switches in the ANPC-DAB converter, as shown in Fig. 1(b). Consequently, in [19], [20], and [21], the ANPC-DAB converter is used to replace the DNPC-DAB converter. However, the numerous power switches and driver circuits are added in the ANPC-DAB converter. The control strategy is complex and the volume and cost are increased.

The HBTL converter is another common structure. Compared to the clamped TL dc–dc converters, the additional clamping diodes, power switches, and flying capacitors are not used and only a dc blocking capacitor is added in the four-switch HBTL dc–dc converter proposed in [22]. There are the advantages of the low cost and compact circuit design. In [23], a capacitor voltage

balancing control method for the HBTL dc–dc converter is proposed to maintain the current balance across the two divided capacitors. The performance and reliability of the converter are improved. In [24], the reasons of voltage imbalance of the blocking capacitor and divided capacitors are analyzed in the HBTL dc–dc converter, and the interleaved PWM modulation strategy is proposed to achieve the voltage. The wide soft switching range is also the key performance to this converter. In [25], an auxiliary MOSFET is added, and the ZVZCS of the main power switches are realized in a wide load range. However, the method results in the high voltage stress on the power switches. In [26], the zero voltage switching (ZVS) range is extended by adding an auxiliary inductor, however, the resonant current is increased under the light load conditions.

The modulation strategy plays the critical role in the TL resonant dc–dc converters and emerged to address the design tradeoffs among ZVS range, current stress, efficiency, and implementation complexity. Conventional single-phase-shift (SPS) or dual-phase-shift modulation strategies are commonly used, but they often suffer from drawbacks such as the limited ZVS range and high current stress. In [27], the phase shift and pulsewidth modulation strategies are designed to realize the buck and boost conversion and ZVS. In [8], the phase shift and variable frequency modulation strategies are used to reduce the rms value of the transformer current in the TL CLLC resonant dc–dc converter. The minimum current trajectory (MCT) modulation strategy is proposed for DAB converter in [28]. In [29], the MCT modulation strategy is applied to three-level resonant converter and the phase-shift angles are optimized to reduce the RMS value of the resonant current under the fixed-frequency operation. Under the MCT modulation strategy, the high frequency resonant current is in phase with the port voltage. Therefore, the body diodes of the power switches are not conducted in advance and ZVS are not achieved. In addition, outside the boundary of MCT, the modulation strategy degenerates into SPS and the minimum rms values of the resonant current are not ensured. In [9], a three-degrees-of-freedom (3DOF) modulation scheme integrating the phase-shift, duty-cycle, and frequency is proposed for the TL T-type *LLC* converter. However, the ZVS of the secondary power switches is not considered. Based on the MCT modulation strategy, the four-degrees-of-freedom (4DOF) modulation scheme proposed in [30] takes into account the phase margin between voltage and current to achieve ZVS on the secondary side, but it is limited to DAB converters. The two strategies in [9] and [30] improve the performance in terms of ZVS and the current stress, but they lack the closed-form analytical solution and depend on numerical computations performed in advance, making the real-time digital implementation more challenging. Therefore, a unified and analytically solvable modulation strategy that ensures full-range ZVS, minimizes the current stress, and remains suitable for digital control remains still scarce.

In summary, the main problems of the bidirectional isolated TL dc–dc converter are as follows.

1) The fly capacitors and HNPC TL dc–dc converter suffer from the poor reliability and the complex control. The efficiency of DNPC-TL converter is low, especially in high-frequency dc–dc applications. The system volume and cost are increased in ANPC-TL converters due to the numerous power switches.
2) The four-switch HBTL dc–dc converter is only used for the unidirectional power transfer. The multicapacitors voltages balance for the bidirectional power transfer should be solved.
3) The existing modulation strategies do not realize the MCT and full-range ZVS in the entire power and voltage conversion range. The modulation strategy should be further optimized.

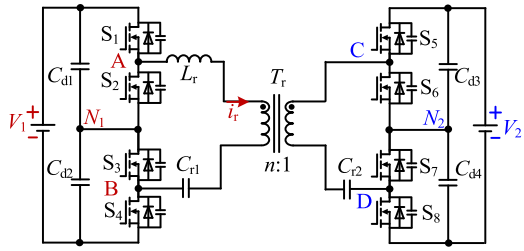

Fig. 2. Proposed bidirectional isolated HBTL resonant DC–DC converter.

To solve the above-mentioned problems, a bidirectional isolated four-switch TL resonant dc–dc converter and its modulation strategy are proposed in this article. The innovations and contributions are as follows. 1) A bidirectional isolated four-switch HBTL resonant dc–dc converter is proposed. The number of power switches is reduced and the clamping power switches, diodes or flying capacitors are removed, therefore the system volume and cost are reduced. 2) A triple-phase-shift compound switching frequency tuning based optimized modulation strategy is proposed to realize the quasi-minimum current trajectory (QMCT) and full ZVS in the entire power and voltage range for the first time.

II. Proposed Converter and Operation Principle

A. Topology and General Modulation Strategy

The proposed dc–dc converter is shown in Fig. 2. The primary side includes the power switches S_1–S_4, the series resonant network with L_{r1} and C_{r1}, and the input divided capacitors C_{d1} and C_{d2}. The secondary side includes the power switches S_5–S_8, the resonant capacitors C_{r2}, and the output divided capacitors C_{d3} and C_{d4}. The turn ratio of the high-frequency transformer T_r is n:1. Ideally, the voltages of the divided capacitors C_{d1} and C_{d2} are half of the input voltage V_1, and the voltages of the divided capacitors C_{d3} and C_{d4} are half of the output voltage V_2. The series resonant networks L_{r1}, C_{r1}, and C_{r2} are used as the intermediate energy storage elements to transfer the power. In addition, C_{r1} and C_{r2} are also used as the isolation capacitors. Therefore, the magnetic flux is balanced between the primary and secondary sides of the transformer.

The circuit structure of the proposed converter is symmetrical and the buck and boost operations are realized in the both power transfer direction. The dual interleaved PWM and phase-shift modulation strategy is used to balance the voltages of the resonant capacitors and control the bidirectional power transfer.

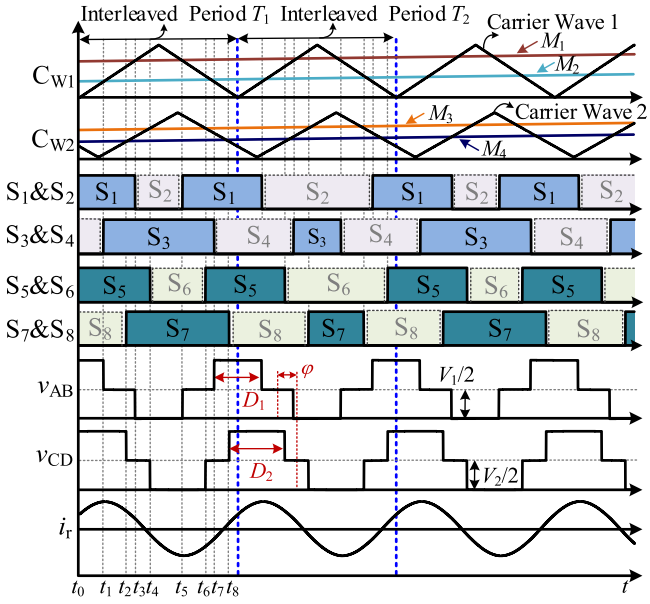

Fig. 3. Key operation waveforms of proposed converter and Interleaved PWM method of the primary side.

The key operation waveforms of the forward mode are shown in Fig. 3, where T represents the switching period. The drive signals for the power switches S_1 and S_2, S_3 and S_4, S_5 and S_6, as well as S_7 and S_8, are complementary, respectively. CW1 and CW2 are the carrier wave, which are used to compare with the modulated wave to generate the driving signal for the switching switches S_1–S_8. The TL waveforms v_{AB} and v_{CD} are generated by controlling the power switches S_1–S_4 and S_5–S_8, whose duty cycles are D_1 and D_2, respectively. The phase shift angle between v_{AB} and v_{CD} is defined as φ. In the proposed converter, $D_1 \in [0, \pi]$, $D_1 \in [0, \pi]$, $\varphi \in [-0.5\pi, 0.5\pi]$. i_r is the high frequency resonant current. The bidirectional power transfer of the proposed converter is controlled by the duty cycles D_1 and D_2, the phase shift angle φ, and the switching frequency f_s.

In the practical application, the discrepancies of control and drive voltages result in the imbalance of the voltages of C_{d1}–C_{d4} and C_{r1} and C_{r2}. Since the proposed converter topology is symmetrical, the voltage balancing method for the secondary-side capacitors can be referred to the primary side, as their mechanisms and implementation approaches are similar. The Interleaved PWM method is used to realize the voltage balance of C_{r1} and C_{r2}. Equation (1) indicates that V_{cr1} is proportional to the duty cycle difference only and is no longer affected by the voltages of the divided capacitors. Although the duty cycle difference is unavoidable in practice, V_{cr1} and V_{cr2} is kept around its ideal value when the Interleaved PWM method is applied [24]

$$V_{cr1} = 0.5\,(V_{cr,PWM1} + V_{cr,PWM2}) = 0.5\,[1 + (D_p - D_n)]\,V_1. \tag{1}$$

Then, only the divided capacitor voltages need to be balanced, which can be achieved by adjusting the phase shift between the carrier wave 1 and the carrier wave 2. If V_{cd2} is less than $V_1/2$, the phase of the carrier wave 2 will be advanced, otherwise it will be delayed. The balancing of the divided capacitor voltages is achieved by the fine-tuning the phase differences between the high and low levels of v_{AB} and v_{CD}, respectively.

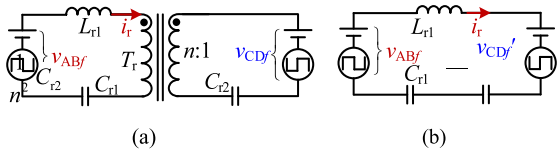

Fig. 4. Equivalent circuit of proposed converter. (a) Equivalent circuit. (b) Equivalent circuit after normalization.

B. Power Characteristics

To simplify the analysis, the power characteristics of the proposed converter are analyzed by the fundamental harmonic analysis method. The equivalent circuit of the proposed converter is shown in Fig. 4(a). v_{ABf} and v_{CDf} are the fundamental components of v_{AB} and v_{CD}, respectively. v_{ABf} and v_{CDf} are expressed as (2) and (3), respectively

$$v_{ABf} = \frac{V_1}{2} + \frac{2V_1}{\pi}\sin\left(\frac{D_1}{2}\right)\sin(\omega_s t) \tag{2}$$

$$v_{CDf} = \frac{V_2}{2} + \frac{2V_2}{\pi}\sin\left(\frac{D_2}{2}\right)\sin(\omega_s t - \varphi). \tag{3}$$

The impedance parameters are imputed to the primary side, and the equivalent circuit of the proposed converter is shown in Fig. 4(b). The equivalent impedance is written as

$$jZ_r = j\left[\omega_s L_{r1} - 1/(\omega_s C_{r1}) - n^2/(\omega_s C_{r2})\right]. \tag{4}$$

The resonant frequency f_r of the resonant circuit is calculated as

$$f_r = 1/\left(2\pi\sqrt{L_{r1}\frac{C_{r1}C_{r2}}{n^2 C_{r1} + C_{r2}}}\right). \tag{5}$$

Thus, the resonant current i_r is expressed as

$$i_r = \frac{2V_1}{\pi Z_r}\left[M\sin\left(\frac{D_2}{2}\right)\cos(\omega_s t - \varphi) - \sin\left(\frac{D_1}{2}\right)\cos(\omega_s t)\right]. \tag{6}$$

where $M = nV_2/V_1$. Based on (2)–(3) and (6), the average power of the proposed converter is derived as

$$P = \frac{2nV_1V_2}{\pi^2 Z_r}\sin\left(\frac{D_1}{2}\right)\sin\left(\frac{D_2}{2}\right)\sin(\varphi). \tag{7}$$

The power transfer expression of the proposed converter is given by (7). According to (7), the maximum power of the proposed converter is $P_{max} = 2nV_1V_2/(\pi^2 Z_r)$. Based on (7), it is seen that the sign of the external phase-shift angle φ determines the direction of power transfer. When $\varphi > 0$, the converter operates in the forward power transfer mode, as illustrated in Fig. 3. Conversely, when $\varphi < 0$, the converter operates in the backward mode. When the reference power transfer is negative, the solved value of the external phase-shift angle φ is also negative. Analogous to the characteristics of the half-bridge DAB converter, the proposed converter is regarded as the cascade of the buck-boost converter according to Fig. 4 and the bidirectional buck-boost conversion is realized. By combining (4) and (7), the power of the proposed converter is controlled by adjusting D_1, D_2, φ, and f_s.

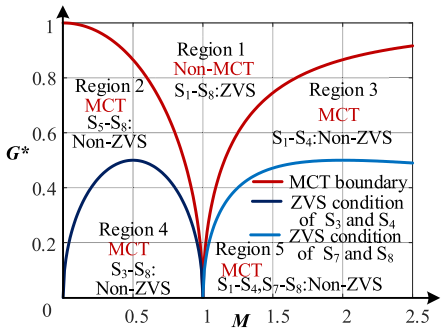

Fig. 5. Optimization results of MCT modulation strategy under different G^* and M.

III. Optimization Modulation Strategy to Realize QMCT and Full Range ZVS

The proposed converter is a typical resonant converter. In [28] and [29], the MCT modulation strategy based on the three phase angles is proposed to minimize the rms value of the high frequency resonant current. In theory, this modulation strategy is also suitable for the proposed converter. However, by analyzing the operation principle of the MCT modulation strategy, the full range ZVS of the switches are not realized. In [30], the 4DOF modulation considers the phase margin between voltage and current to achieve ZVS on the secondary side, but it lacks the closed-form analytical solution. And the wide frequency variation range poses the challenges for the magnetic component design. Therefore, it is necessary that an analytically solvable optimized modulation strategy based on the four variables D_1, D_2, φ, and f_s is proposed to realize the full range ZVS and quasi-minimum RMS value of the high frequency resonant current at the same time.

A. Analysis of MCT and 4DOF Modulation Strategies

In this section, the limitations of the MCT modulation strategy and 4DOF modulation strategy are analyzed in detail.

In [8], the rms value of the high frequency resonant current is minimized by the Karush-Kuhn-Tucker conditions Under different values of G^* and M, the optimization results of the MCT modulation strategy are illustrated in Fig. 5. G^* represents the ratio of the desired power P^* to the maximum power $P_{\max}$, and G^* is expressed as

$$G^* = P*/P_{\max} = \sin(0.5D_1)\sin(0.5D_2)\sin(\varphi). \quad (8)$$

The maximum transfer power $P_{\max}$ is precalculated based on the circuit parameters, as shown in (7). The normalized $|G|$ is a fixed value between 0 and 1. Although the expected transfer power (i.e., G) is the same, the control variables differ due to the different constraint considerations. Consequently, the converter operates under the different conditions, resulting in the different resonant current stress, ZVS condition and efficiencies.

The constraint conditions of MCT strategies are the transfer power and minimum RMS value of i_r. Taking $M<1$ as an example. The operation principle of the MCT modulation strategy is analyzed. Phasor diagrams of MCT modulation strategy are shown in Fig. 6. In Fig. 6(a), for the given transfer power, all three conditions (①, ②, and ③) can achieve the same power.

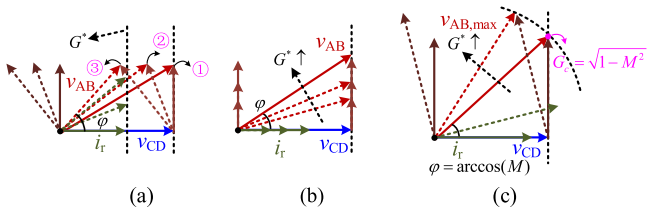

Fig. 6. Phasor diagrams of MCT modulation strategy. (a)Realization of MCT under the given G^*. (b) right-angled triangle is formed as G^* increases. (c) SPS (Boundary condition).

However, the method in ①, which forms a vector triangle, corresponds to the MCT modulation strategy. The hypotenuse is $v_{\rm AB}$, the phase of i_r is matched with that of $v_{\rm CD}$. In the situation, the RMS value of i_r is minimized. In phase two, as the transfer power increases, the length of $v_{\rm AB}$ increases, and its endpoint slides down the vertical line, maintaining a right-angled triangle, as shown in Fig. 6(b). However, with the power increasing, there is a boundary condition of MCT, as shown in Fig. 6(c). When $v_{\rm AB}$ reaches its maximum, if the desired power P^* increases, the vector right angled triangle is not formed and the phase of i_r is not matched with that of $v_{\rm CD}$. Beyond the boundary conditions, the MCT modulation strategy degenerates into single phase shift and the length of $v_{\rm AB}$ is same in [8]. Therefore, the minimum rms value of i_r is not realized when $G^* > \sqrt{1-M^2}$.

Then, the ZVS range under the MCT modulation strategy is analyzed. In the ON-state, the $v_{\rm ds}$ of the MOSFET is close to zero. During turn-OFF, the voltage begins to rise while the current decreases. Due to the presence of parasitic capacitors, when MOSFET is turned OFF, $v_{\rm ds}$ is approximately zero. Then, zero-voltage OFF (ZV-OFF) is approximately considered naturally achieved. Therefore, the main focus of the modulation strategy is on achieving zero-voltage ON (ZV-ON). It is known that zero voltage ON is realized if the body diode is conducted before the corresponding power switch is turned ON. According to Fig. 3, the ZV-ON conditions for the power switches S_1–S_4 and S_5–S_8 are expressed as

$$\begin{cases} S_1, S_2 : i_r(t_5) = i_r\left(-\pi/2 + D_1/2\right) < 0 \\ S_3, S_4 : i_r(t_7) = i_r\left(\pi/2 - D_1/2\right) < 0 \\ S_5, S_6 : i_r(t_6) = i_r\left(\varphi\right) > 0 \\ S_7, S_8 : i_r(t_8) = i_r\left(\varphi\right) > 0 \end{cases}. \quad (9)$$

Based on the above-mentioned analysis, the phase relationship about $v_{\rm AB}$, $v_{\rm CD}$, and i_r is shown in Fig. 7 under the MCT modulation strategy. During the light load, phasor diagrams and time domain waveforms of $v_{\rm AB}$, $v_{\rm CD}$, and i_r are illustrated in Fig. 7(a) and (b). The power switches S_3–S_8 are hard switching. As shown in Fig. 7(c) and (d), as the desired power increases, the ZV-ON conditions for the power switches S_3–S_4 are met. However, although the RMS value of i_r are minimized on the MCT, the phase matching between i_r and $V_{\rm CD}$ results in $i_r(t_6) = i_r(t_8) = 0$. Therefore, the body diodes of the power switches S_5–S_8 are not be conducted before the corresponding power switches are gated ON. The ZVS of the power switches S_5–S_8 are not realized. As G^* increases to the boundary condition of MCT, the MCT modulation strategy degenerates into single phase shift, as shown in Fig. 7(e) and (f). Therefore, the minimum RMS value of i_r is not realized outside the boundary

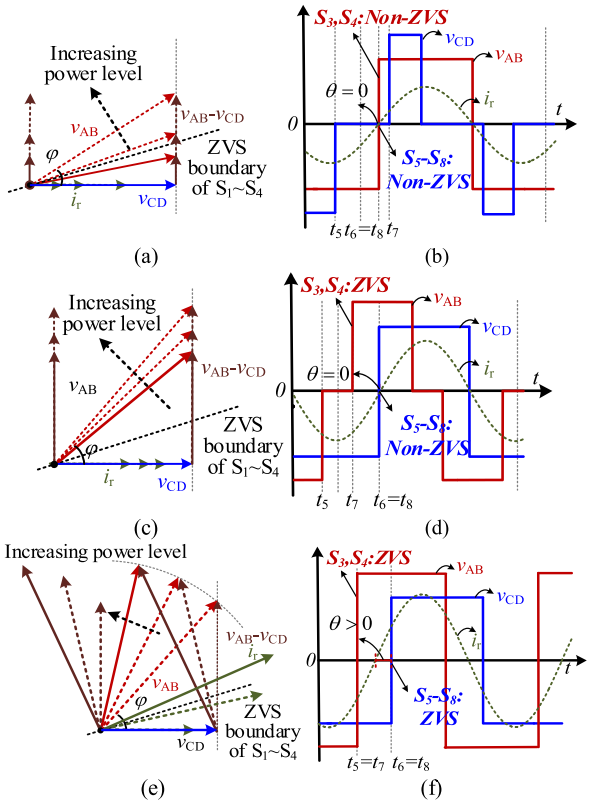

Fig. 7. Phase relationship between v_{AB}, v_{CD}, and resonant current When $M<1$ under MCT modulation strategy. (a) Phasor diagram in light load. (b) Time domain waveforms in light load. (c) Phasor diagram in MCT. (d) Time domain waveforms in MCT. (e) Phasor diagram outside boundary of MCT. (f) Time-domain waveforms outside boundary of MCT.

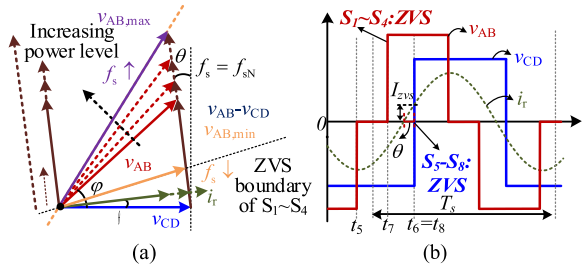

Fig. 8. Phase relationship between v_{AB}, v_{CD}, and resonant current when $M<1$ under proposed modulation strategy in fixed frequency. (a) Phasor diagram. (b) Time domain waveforms.

of MCT. A similar conclusion is drawn for the case when $M>1$.

In summary, although the RMS value of the resonant current is minimized, the phase between v_{CD} and i_r is matched under the traditional MCT modulation. The resonant current i_r is zero due to the phase matching when the power switches on the phase-matched side turn ON or turn OFF. When parameter accuracy is compromised, the resonant current i_r may either exceed zero or fall below zero, both of which can affect the ZVS condition. When i_r is less than zero, the body diodes conduct in advance, allowing for soft switching and meeting the ZVS condition. However, when i_r is greater than zero, the body diodes of the power switches do not conduct in advance, preventing ZVS, and the MCT modulation strategy is not automatically correct this deviation. Moreover, as G^* decreases, the ZVS range of the power switches in the nonphase-matched side is further limited. As G^* increases, the MCT modulation strategy degrades and the current stress of i_r increases.

In addition, the 4DOF modulation strategy proposed in [30] based on MCT method introduces four independent control variables: two phase-shift angles, duty cycle, and switching frequency. By controlling the phase margin between the port voltage and resonant current, it enables ZVS ON the secondary-side power switches while simultaneously reducing the rms value of i_r, thereby improving the efficiency. However, several notable limitations remain. First, the modulation strategy lacks the closed-form analytical solutions, relying on the precomputed lookup tables or offline numerical optimization. Second, to ensure the power regulation and ZVS operation, this method operates over very wide switching frequency range, which poses the challenges for the design of magnetic components. The 4DOF modulation strategy still suffers from the limitations in terms of the analytical tractability, implementation complexity, and real-time feasibility. Therefore, the analytical method of reducing the rms value of high-frequency resonant current while achieving the full ZVS range with the narrow frequency variation should be deeply researched.

B. *Principle of Proposed Optimized Modulation Strategy*

Based on the above-mentioned analysis, due to the phase matching, the body diodes are not turned ON before i_r reaches zero under the MCT modulation strategy. Consequently, minimizing the rms of the resonant current is in contradiction with achieving the ZVS. Therefore, how to realize the full-range quasi-minimum rms value of i_r needs to be researched, meanwhile, the full-range ZVS is ensured.

In this section, the full-range ZVS modulation strategy based on the QMCT is proposed and introduced as follows.

Taking $M<1$ as an example, in the region 2 of Fig. 5, by controlling D_1, D_2, and φ, i_r is controlled to keep slightly ahead of V_{CD}. The zero-crossing is occurred after the moment t_3, as shown in Fig. 8(a) and (b). Based on the method, the quasi-minimum rms value of i_r is realized while the ZVS for S_1–S_8 is ensured. Therefore, the efficiency of the proposed converter is obviously improved. In this case, only D_1, D_2, and φ need to be controlled.

As G^* decreases, D_1 and φ are reduced and the ZV-ON conditions for the power switches S_3–S_4 are not met. At this situation, D_1, D_2, and φ have already been calculated and determined to realize the quasi-minimum rms value of i_r. However, the primary power switches S_3 and S_4 are not achieve ZVS unless a new degree of freedom is introduced. Through analysis, f_s is the only remaining degree of freedom for the proposed converter. As shown in Fig. 9(a) and (b), when G^* decreases to the non-ZVS region of S_3 and S_4, f_s is increased to raise the resonant impedance and reduce the power. Then, D_1 and φ are correspondingly increased to ensure that S_3 and S_4 realize ZVS. Similarly, when G^* increases to the boundary condition of the QMCT, f_s is decreased to reduce the resonant impedance and improve the power, as shown in Fig. 10(a) and (b). In this way,

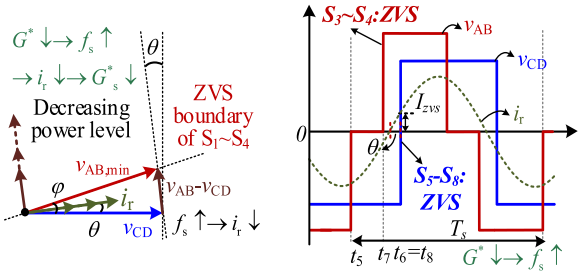

Fig. 9. Phase relationship between v_{AB}, v_{CD}, and i_r in increasing frequency region when $M<1$ under proposed modulation strategy. (a) Phasor diagram. (b) Time domain waveforms.

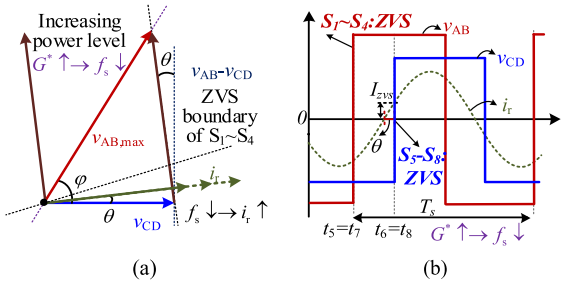

Fig. 10. Phase relationship between v_{AB}, v_{CD}, and i_r in decreasing frequency region when $M<1$ under proposed modulation strategy. (a) Phasor diagram. (b) Time domain waveforms.

the ZVS of all power switches and the quasi-minimum RMS value of i_r are achieved simultaneously.

Next, the proposed modulation strategy is calculated and derived. Under the given desired power P^*, the junction capacitors C_{oss} of the secondary power switches need to be fully discharged by the resonant current i_r to realize the ZVS. The phase difference between V_{CD} and i_r is defined as θ. Under the constraint of ZVS for the secondary power switches, angle θ meets

$$\theta \geq \arctan\left[2V_2^2 C_{oss}/(\pi P^* T_d)\right]. \tag{10}$$

In (10), T_d is the dead time. The minimum constraint in (10) need to be satisfied. Typically, since the junction capacitors C_{oss} of the power switch is quite small, the calculated phase difference θ is approximately 1–10°. θ is selected to ensure the efficient operation across a wide range of load conditions while maintaining ZVS. In addition, considering the impact of the practical parameters, the theoretical value of θ may differ from the actual value, and adjustments to θ can be made to correct for such differences, increasing the flexibility of the proposed modulation strategy. In the practical condition, θ needs to be selected with a compromise. The rms value of the resonant current will be increased if the θ is too large. However, ZVS for the power switches will not be realized if the θ is too small.

In the proposed full-range ZVS modulation strategy based on the QMCT, the corresponding θ is calculated based on (10) under P^*. Therefore, θ is regard as a known constant. In the region 2 of the proposed modulation strategy, D_1, D_2, and φ are controlled, and f_s is constant. In the region 3, D_1, D_2, φ, and f_s are controlled to achieve the quasi-minimum rms value of the high-frequency resonant current and full range ZVS of power switches simultaneously.

The method of seeking the corresponding D_1, D_2, φ, and f_s based on G^*, θ, and the relevant circuit parameters is the key to the proposed optimized modulation strategy. The detailed derivation is as follows.

Taking $M<1$ as an example, the high frequency resonant current i_r is written as

$$i_r = \frac{2V_1}{\pi Z_r}\sqrt{\begin{matrix}[M\sin(\varphi)]^2 \\ +[M\cos(\varphi)-\sin(0.5D_1)]^2\end{matrix}}\sin(\omega_s t+\alpha) \tag{11}$$

where α represents the phase of the resonant current i_r. α is derived as follows:

$$\tan(\alpha) = \frac{M\cos(\varphi)-\sin(0.5D_1)}{M\sin(\varphi)}. \tag{12}$$

The phase of v_{CD} is -φ. When the phase difference between the resonant current i_r and v_{CD} is θ, (13) is obtained

$$\theta - \varphi = \alpha. \tag{13}$$

Both sides in (13) are simultaneously subjected to the tangent function and it is expressed as

$$\tan(\alpha) = \frac{\tan(\theta)-\tan(\varphi)}{1+\tan(\theta)\tan(\varphi)}. \tag{14}$$

Combing (8), (12), and (14), after the simplification, the following equation is calculated and derived as follows:

$$\frac{\tan(\theta)\cos(\varphi)-\sin(\varphi)}{\cos(\varphi)+\tan(\theta)\sin(\varphi)} = \frac{M\sin(\varphi)\cos(\varphi)-G^*}{M\sin^2(\varphi)}. \tag{15}$$

Based on (7) and (15), since $|\sin(0.5D_1)| \leq 1$and $|\sin(\varphi)| \leq 1$, D_1, D_2, and φ are further obtained as

$$\begin{cases} \text{if } |G^*| \leq \sqrt{1-M^2} \\ D_1 = 2\arcsin\left(\sqrt{(A^2+1)G^{*2}+M^2-2AMG^*}\right) \\ D_2 = \pi, f_s = f_{sN} \\ \varphi = \arcsin\left(\frac{G^*}{\sqrt{(A^2+1)G^{*2}+M^2-2AMG^*}}\right) \end{cases} \tag{16}$$

where A = tan(θ). The difference and the advantage are that the quasi-minimum RMS value of i_r and full-range ZVS of power switches are simultaneously achieved in the region defined by (16). Next, the ZVS conditions under the QMCT modulation strategy are analyzed. By combining (9), (11), and (16), under the proposed modulation strategy, the full range ZVS of S_1–S_2 and S_5–S_8 are achieved. However, the ZVS condition for S_3 and S_4 is expressed as

$$(A^2+1)G^{*2}+M^2-2AMG^* \geq \sqrt{A^2G^{*2}+M^2-2AMG^*}. \tag{17}$$

Since $A = \tan(\theta)$ is relatively small, (17) is simplified to

$$|G^*| \geq \sqrt{M-M^2}. \tag{18}$$

When $|G^*| < \sqrt{M-M^2}$, the quasi-minimum rms value of the high-frequency resonant current and full-range ZVS of all of the power switches are achieved by D_1, D_2, and φ obtained from (19). In this region, the variable frequency modulation is not used. However, when$|G^*| < \sqrt{M-M^2}$, the ZVS of S_3

and S_4 are not achieved. In this case, as the above-mentioned analysis, the switching frequency f_s is introduced as an additional degree of freedom, and D_1, D_2, and φ are confined within the region $|G^*| \geq \sqrt{M-M^2}$. In order to minimize the range of frequency variation and simplify the modulation strategy, D_1, D_2, φ are determined based on the ZVS critical conditions$|G_c| = \sqrt{M-M^2}$, as shown in (18). f_{sN} is the rated switching frequency.

Next, the new switching frequency $f_s{}^*$ need to be derived. At the switching frequency $f_s{}^*$, there are

$$\begin{cases} G^* P_{\max} = \frac{2nV_1V_2}{\pi^2 Z_r^*} \sin(\frac{D_1}{2}) \sin(\frac{D_2}{2}) \sin(\varphi) \\ Z_r^* = \omega_s^* L_{r1} - 1/(\omega_s^* C_{r1}) - n^2/(\omega_s^* C_{r2}) \end{cases} \tag{19}$$

where $Z_r{}^*$ is the corresponding impedance of the switching frequency $f_s{}^*$. By combining (4), (5), (16), and (19), the proposed modulation strategy when $|G^*| < \sqrt{M-M^2}$ is further optimized as

$$\begin{cases} \text{if } |G^*| \leq \sqrt{M-M^2} \\ G_c = \sqrt{M-M^2}, D_1 = \pi \\ D_2 = 2\arcsin\left(\sqrt{(A^2+1){G_c}^2 + M^2 - 2AMG_c}\right) \\ \varphi = \arcsin\left(G_c/\sqrt{(A^2+1){G_c}^2 + M^2 - 2AMG_c}\right) \\ f_s^* = \frac{A_s+\sqrt{A_s^2+4}}{2} f_r, A_s = \frac{G_c}{|G^*|}\left(\frac{f_{sN}}{f_r} - \frac{f_r}{f_{sN}}\right) \end{cases} \tag{20}$$

$$\begin{cases} \text{if } |G^*| > \sqrt{1-M^2} \\ G_q = \sqrt{1-M^2}, D_1 = \pi \\ D_2 = 2\arcsin\left(\sqrt{(A^2+1){G_q}^2 + M^2 - 2AMG_q}\right) \\ \varphi = \arcsin\left(G_q/\sqrt{(A^2+1){G_q}^2 + M^2 - 2AMG_q}\right) \\ f_s^* = \frac{A_s+\sqrt{A_s^2+4}}{2} f_r, A_s = \frac{G_q}{|G^*|}\left(\frac{f_{sN}}{f_r} - \frac{f_r}{f_{sN}}\right) \end{cases} . \tag{21}$$

Similarly, when $M>1$, the proposed optimized modulation strategy is derived as

$$\begin{cases} \text{if } |G^*| > \sqrt{1-1/M^2} \\ G_q = \sqrt{1-1/M^2}, D_1 = 1 \\ D_2 = 2\arcsin\left(\sqrt{1+A^2M^2{G_q}^2 + M^2{G_q}^2 - 2AMG_q}/M\right) \\ \varphi = \arcsin\left(MG_q/\sqrt{1+A^2M^2{G_q}^2 + M^2{G_q}^2 - 2AMG_q}\right) \\ f_s^* = \frac{A_s+\sqrt{A_s^2+4}}{2} f_r, A_s = \frac{G_q}{|G^*|}\left(\frac{f_{sN}}{f_r} - \frac{f_r}{f_{sN}}\right) \end{cases} \tag{22}$$

$$\begin{cases} \text{if} \sqrt{1/M-1/M^2} \leq |G^*| \leq \sqrt{1-1/M^2} \\ f_s^* = f_{sN}, D_1 = \pi \\ D_2 = 2\arcsin\left(\frac{\sqrt{1+A^2M^2{G^*}^2 + M^2{G^*}^2 - 2AMG^*}}{M}\right) \\ \varphi = \arcsin\left(MG^*/\sqrt{1+A^2M^2{G^*}^2 + M^2{G^*}^2 - 2AMG^*}\right) \end{cases} \tag{23}$$

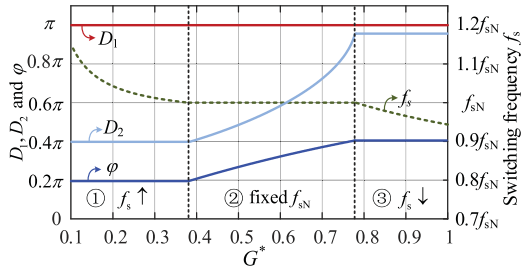

Fig. 11. Curve graph of control parameters D_1, D_2, φ, and switching frequency f_s with $G*$ when $M<1$.

$$\begin{cases} \text{if } |G^*| \leq \sqrt{1/M-1/M^2} \\ G_c = \sqrt{1/M-1/M^2}, D_1 = 1 \\ D_2 = 2\arcsin\left(\frac{\sqrt{1+A^2M^2{G_c}^2 + M^2{G_c}^2 - 2AMG_c}}{M}\right) \\ \varphi = \arcsin\left(MG_c/\sqrt{1+A^2M^2{G_c}^2 + M^2{G_c}^2 - 2AMG_c}\right) \\ f_s^* = \frac{A_s+\sqrt{A_s^2+4}}{2} f_r, A_s = \frac{G_c}{|G^*|}\left(\frac{f_{sN}}{f_r} - \frac{f_r}{f_{sN}}\right) \end{cases} . \tag{24}$$

And the backward and forward modes are symmetrical, and the distinction lies in the sign of the external phase-shift angle φ. Under the backward mode, D_1, D_2, φ, and the switching frequency f_s are obtained by (20)–(24), but it is noted that the external phase-shift angle φ is negative.

Curve graph of control parameters D_1, D_2, φ, and switching frequency f_s with $G*$ when $M<1$ is drawn in Fig. 11. In the fixed-frequency region (Region ②), the switching frequency f_s is set to the rated switching frequency f_{sN}, and the shift-phases D_1, D_2, φ are determined based on the constraints of the desired power, ZVS and quasi-minimum rms value of the resonant current. Outside the boundary condition—that is, in Regions ② and ③, the switching frequency control is introduced according to the precalculated boundary conditions to satisfy the aforementioned constraints. In this way, both quasi-minimum rms value of the resonant current and full ZVS are achieved simultaneously. The case when $M>1$ is similar.

C. Comparison With MCT Modulation Strategy

Under the different P^*, the values of D_1, D_2, φ, and f_s are calculated according to (16) and (20)–(24). The QMCT and the MCT for $M = 0.5$ and $M = 1.8$ are drawn in Fig. 12. When $M\leq 1$, for the desired power P^*, two operating points $Q(\gamma 1\text{-})$ and $Q(\gamma 1\text{+})$ are located on the $\gamma 1$- and $\gamma 1$+ branches of the QMCT, as illustrated in Fig. 12(a). The two points are physically equivalent and they correspond to the same phasor diagrams. The QMCT is approximately elliptical. The proposed QMCT is wider than that of MCT. The situation is similar when $M>1$, as shown in Fig. 12(b).

Frequency variation graphs surfaces under different G^* and M under the proposed modulation strategy are drawn in Fig. 13. The switching frequency is increased under light load. Within the boundaries of the ZVS and QMCT, the switching frequency is fixed and D_1, D_2, and φ are designed to achieve the full range ZVS of the power switches and the quasi-minimum rms of i_r. As

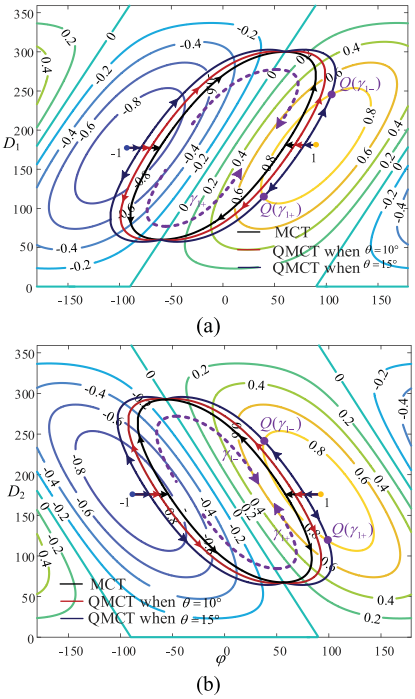

Fig. 12. QMCT and MCT. (a) On $D_2 = 180°$ plane for $M = 0.5$. (b) On $D_1 = 180°$ plane for $M = 1.8$.

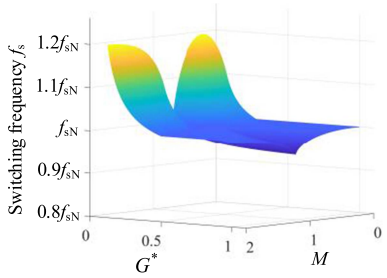

Fig. 13. Three-dimensional distributed curves of the switching frequency as the functions of G^* and M under proposed modulation strategy.

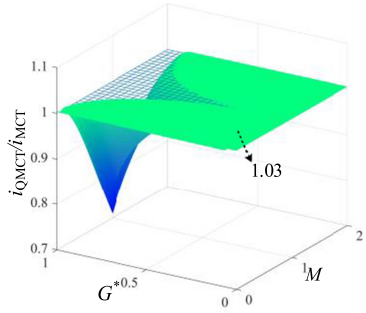

Fig. 14. Surface graphs of ratios of rms of i_r under proposed modulation strategy and that of MCT under different G^* and M.

G^* increases, f_s is decreased to realize the above functions. From Fig. 13, the frequency variation range is 0.9–1.2 times the rated frequency and the design of magnetic components is relatively simple.

Surface graphs of ratios of the rms of i_r under the proposed modulation strategy to that of MCT are drawn in Fig. 14. The full range ZVS is not achieved under the MCT modulation strategy. Outside the boundary of MCT, the MCT modulation strategy degenerates into single phase shift and the minimum rms value of i_r is not ensured. Compared to the MCT modulation strategy, the full range ZVS is achieved at the cost of a 3% increase in current stress in the fixed switching frequency under the proposed optimized modulation strategy. It is worthwhile to achieve the full range ZVS with a slight increase of the rms of the high frequency resonant current. In the region of decreasing the switching frequency, the rms value of i_r is less than that of MCT modulation strategy. Therefore, the full range ZVS of the power switches and the quasi-minimum rms value of the high-frequency resonant current are achieved simultaneously under the proposed optimized modulation strategy. The efficiency of the proposed converter is improved.

IV. Experimental Verification

To verify the bidirectional power transfer characteristics and the proposed optimized modulation strategy, the general half-bridge modules are adopted and the experimental prototype of the proposed bidirectional isolated HBTL resonant dc–dc converter is built, as shown in Fig. 15(a). The system control diagram is shown in Fig. 15(b). The process flow chart of system is presented in Fig. 15(c). The voltages of the divided capacitors C_{d1}, C_{d2}, C_{d3} and C_{d4} are detected and passed to the DSP28377. As shown in Fig. 15(b) and (c), the parameter V_1, V_2, M, and Z_r required for the proposed modulation strategy is calculated based on the circuit parameters. Then, the mode selection is performed based on the value of M. When $M<1$, the control parameters D_1, D_2, φ, and f_s are calculated and gained based on $P*$, (16), (20), and (21). When $M>1$, the control parameters D_1, D_2, φ, and f_s are calculated and gained based on P^* and (22)–(24). The calculated control parameters are transmitted to the FPGA by the communication. For the balancing of the divided capacitor voltages, the sampled voltages are sorted. The sorted voltages are compared to determine whether the carrier signal should be led or delayed. The corresponding carrier phase shift (advance or delay) information is then transmitted to the FPGA. Based on the above-mentioned information, the FPGA generates all the PWM signals for the power switches. Finally, all power switches are controlled by the isolated driven circuits. In this way, both the proposed modulation strategy and the dynamic balancing of the divided capacitor voltages are achieved.

The experimental parameters are presented in Table I. Apart from the balancing control of the voltages of the capacitors, the experimental verification is conducted under the open-loop conditions.

A. Experiment Waveforms

First, the proposed modulation strategy is verified in the forward mode. Under the different desired power P^*, the switching period level waveforms of the MCT and the proposed optimized modulation strategy are shown in Figs. 16 and 17, respectively. When $P^* = 1600$ W and $P^* = 2000$ W, the steady-state waveforms of the MCT modulation strategy and the proposed optimized full-range ZVS modulation strategy based on QMCT

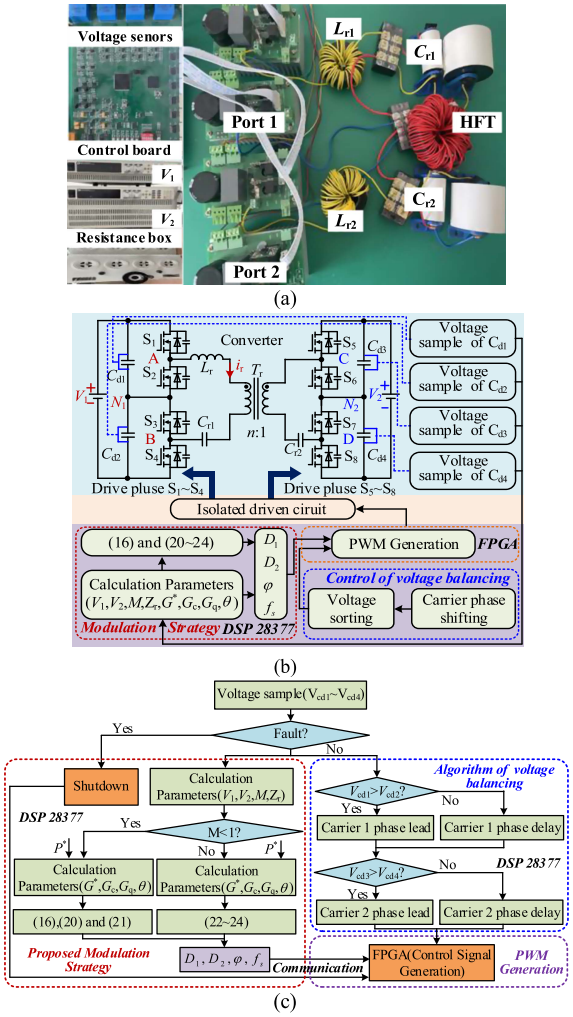

Fig. 15. Experimental prototype of proposed converter and diagram of control system. (a) Experimental prototype. (b) Diagram of control system. (c) Process flowchart.

TABLE I
EXPERIMENTAL PARAMETERS

Names of parameters	Values of parameters
Input voltage (V_1)	400V/800V
Output voltage (V_2)	200V/400V
Rated switching frequency (f_{sN})	50kHz
Range of switching frequency (f_s)	49kHz~65kHz
Turn ratio of transformer (n:1)	1:1
Resonant inductance (L_{r1})	208μH/249uH
Resonant capacitances (C_{r1}, C_{r2})	110nF/200nF
Divided capacitances (C_{d1}~C_{d4})	220μF
Type of power switches	IPW60R070C6
Deadtime (T_d)	300ns

are presented in Figs. 16 and 17, respectively. The experimental values of D_1, D_2, φ, and f_s are almost the same as the theoretical calculation results. In Fig. 16(a), the ZVS for S_5–S_8 is not achieved under the MCT modulation. However, under the proposed optimized modulation strategy, the ZVS of all power switches and the quasi-minimum rms value of i_r are achieved simultaneously, as shown in Fig. 16(b). In Fig. 17(a), when $P^* =$ 2000 W, the MCT modulation strategy degenerates into single

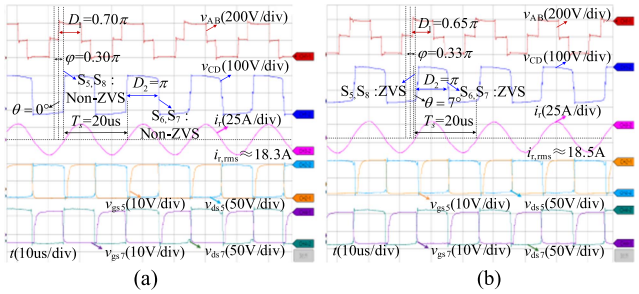

Fig. 16. Experimental waveforms when $P^* = 1600$ W in forward mode. (a) MCT. (b) Proposed.

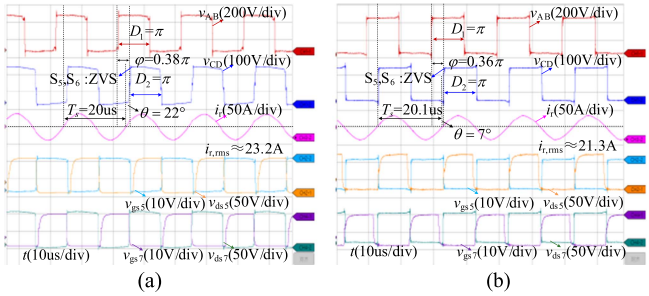

Fig. 17. Experimental waveforms when $P^* = 2000$ W in forward mode. (a) MCT. (b) Proposed.

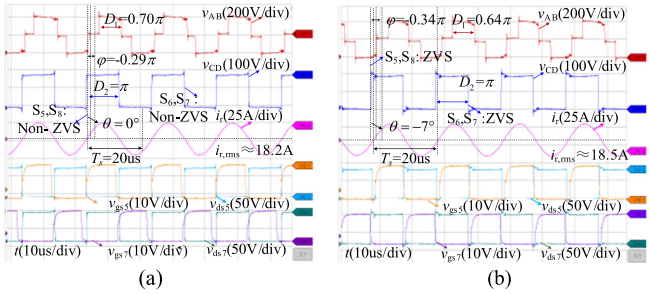

Fig. 18. Experimental waveforms when $P^* = -1600$ W in backward mode. (a) MCT. (b) Proposed.

phase shift and the minimum rms value of i_r is not ensured. However, under the proposed modulation strategy, the rms value of i_r is reduced by 10% and the ZVS of all power switches is realized, as illustrated in Fig. 17(b). The voltage stresses on all power switches are limited to half of the input or output voltage. The advantages of the proposed converter and the optimized modulation strategy are verified in the forward mode.

Next, the proposed optimized modulation strategy is verified in the backward mode. When $P* =$ -1600 W, the steady-state waveforms of the MCT modulation strategy and the proposed modulation strategy are presented in Fig. 18(a) and (b), respectively. In Fig. 18(a), the ZVS for the secondary power switches S_5–S_8 is not achieved. However, under the proposed optimized modulation strategy, the ZVS of all power switches is achieved, and the rms value of i_r is approximately equal to that of MCT. When $P^* =$ -2000 W, the MCT modulation strategy is degenerated and the rms value of i_r increases, as shown in Fig. 19(a). However, as shown in Fig. 19(b), under the proposed modulation strategy, the quasi-minimum rms value of i_r and the

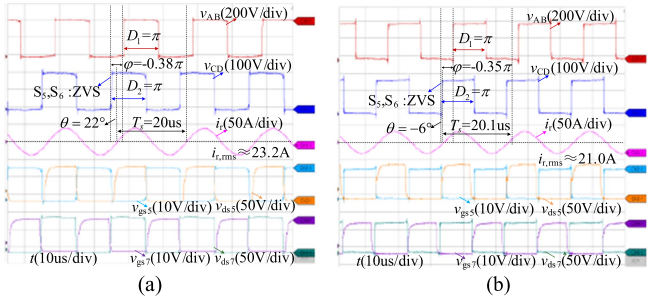

Fig. 19. Experimental waveforms when $P^*=-2000$ W in backward mode. (a) MCT. (b) Proposed.

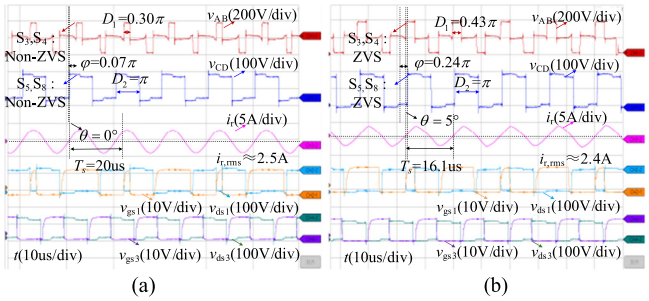

Fig. 20. Experimental waveforms when $P^*=200$ W under light load. (a) MCT. (b) Proposed.

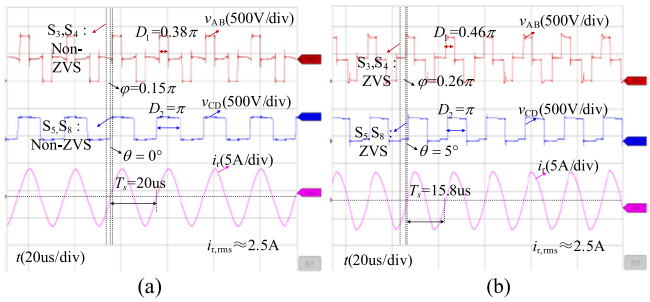

Fig. 21. Experimental waveforms under high input voltage when $P^*=400$ W under light load. (a) MCT. (b) Proposed.

ZVS of all of the power switches are realized simultaneously. The effectiveness of the proposed modulation strategy is verified in the backward mode.

Under the light load, when $P^*=200$ W, corresponds to 10% of the maximum power, the steady-state waveforms of the MCT modulation strategy and the proposed optimized full-range ZVS modulation strategy based on QMCT are shown in Fig. 20(a) and (b), respectively. In Fig. 20(a), the ZVS of the power switches S_3–S_8 is not achieved under the MCT modulation strategy. However, by introducing the QMCT and the frequency variation, the ZVS of all power switches is achieved under the proposed modulation strategy, meanwhile the rms value of the resonant current i_r is close to that of MCT. The effectiveness of the proposed modulation strategy is verified under the light load.

To further enhance the persuasiveness of the proposed strategy, the input voltage is increased to 800 V. The corresponding experimental waveforms are shown in Figs. 21 and 22. As can be seen from Figs. 21 and 22, the proposed modulation strategy, based on the closed-form analytical solution with four degrees

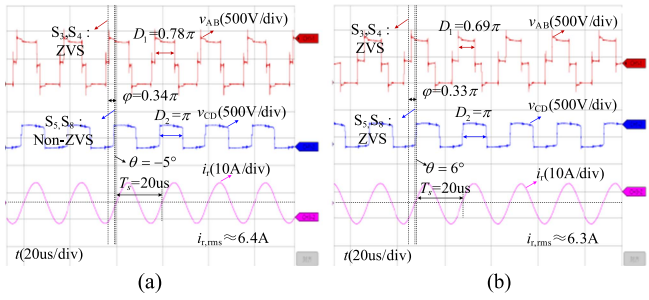

Fig. 22. Experimental waveforms under high input voltage when $P^*=1100$ W under light load. (a) MCT. (b) Proposed.

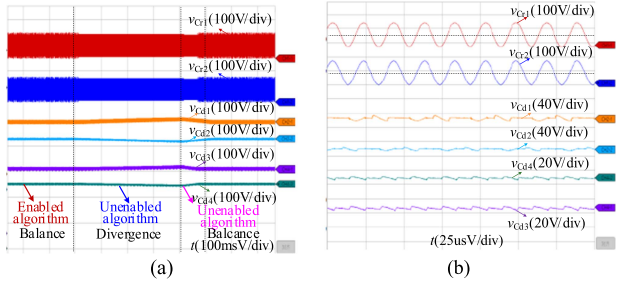

Fig. 23. Capacitor voltage balancing experimental waveforms. (a) Voltages of divided capacitors. (b) Voltages of resonant capacitors.

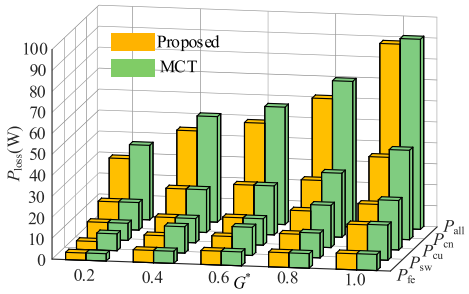

Fig. 24. Bar chart of loss distribution between the proposed modulation strategy and MCT modulation strategy under the different transfer power.

of freedom, achieves the quasi-minimum rms resonant current while maintaining ZVS for all power switches. The results further verify the effectiveness of the proposed strategy under the high voltage levels.

In addition, the voltages V_{cd1}–V_{cd4} of the divided capacitors and the voltages V_{cr1} and V_{cr2} of the resonant capacitors are dynamically balanced, as shown in Fig. 23. Therefore, the effectiveness of the balance of the voltages of the divided capacitors and resonant capacitors are verified.

B. Comparison

Furthermore, the proposed converter is compared with the other bidirectional isolated TL dc–dc converters, as shown in Table II. In the T-type TL converter in [9], the voltage stresses on the power switches are high. The cost of the DNPC-DAB converter in [12] is low. However, the distribution of the power loss is unbalanced and the ZVS range is limited. Therefore, the efficiency of the converter is reduced. There are the numerous diodes and clamping capacitors in the HNPC-DAB converter in [16]. The reliability of this converter is reduced by frequently

TABLE II
COMPARISON WITH OTHER BIDIRECTIONAL ISOLATED TL DC–DC CONVERTERS

Converter	Number of Components			Voltage Stress on Primary	Voltage Stress on Secondary	ZVS Range	Current Stress	Efficiency
	Switches	Diodes	Capacitors					
[9]	8	0	5	V_{in}	V_o	Relatively Wide	Relatively	97.2%@2kW
[12]	16	8	4	$0.5V_{in}$	$0.5V_o$	Narrow	Low	94%@90kW
[16]	8	4	6	$0.5V_{in}$	$0.5V_o$	Relatively Wide	High	95.8%@2kW
[20]	12	0	4	$0.5V_{in}$	$0.5V_o$	Wide	High	92%@1kW
[21]	12	0	4	$0.5V_{in}$	$0.5V_o$	Wide	High	94.5%@1kW
[29]	8	0	4	V_{in}	V_o	Narrow	Low	94%@1kW
Proposed	8	0	6	$0.5V_{in}$	$0.5V_o$	Wide	Medium	96.3%@2kW

TABLE III
COMPARISON WITH OTHER MODULATION STRATEGIES

Parameters	[28]	[30]	[9]	[31]	Proposed
Topology	TL-LC+LC-TL	CF-FB+ F-HBTL	T-Type LLC	DAB	F-HBTL
Modulation Strategy	VFM+PSM	MCT	3DOF	4DOF	QMCT+ZVS
Degrees-of-Freedom	2 (D_1, f_s)	3 (D_1, D_2, φ, f_s)	3 (D_1, φ, f_s)	4 (D_1, D_2, φ, f_s)	4 (D_1, D_2, φ, f_s)
Closed-form Analytical Solution	Yes	Yes	No	No	Yes
Table Look-up	No	No	Yes	Yes	No
Computational Complexity	Low	Medium	High	High	Medium
Current Stress	Global Minimum	Part Minimum	Global Minimum	Global quasi-Minimum	Global quasi-Minimum
Buck-Boost Conversion	$M<1$	$M<1$ or $M>1$	$M<1$	$M<1$ or $M>1$	$M<1$ or $M>1$
ZVS of Primary Side	Part	Part	All	All	All
ZVS of Secondary Side	No	No	No	All	All
Frequency Range	Wide	Fixed	Wide	Wide	Narrow

charging and discharging of the clamping capacitors. Compared to the ANPC converters in [20] and [21], there are only eight power switches and the volume and cost are reduced in the proposed converter. In terms of current stress, the full-bridge converters presented in [12] and [28] exhibit the lowest stress levels. The converters in [9], [20], and [21], as well as the proposed topology, adopt the half-bridge structure. Due to the introduction of switching frequency as an additional degree of freedom in [9] and the proposed modulation, the resulting current stress is lower than that in [20] and [21]. However, the proposed converter achieves the reduced voltage stress compared to [9]. The full-range ZVS is realized in the proposed converter and the efficiency of the proposed converter reaches 96%. The two-level structure is still used in the hybrid current-fed isolated bidirectional series resonant dc–dc converter in [27]. The voltage stresses on the power switches are increased. The ZVS ranges of the power switches are limited under the MCT modulation strategy in [27]. In summary, there are more advantages in the bidirectional power transfer, ZVS range, cost, and efficiency in the proposed converter.

Then, the proposed modulation strategy is compared with other modulation strategies, as shown in Table III. The MCT modulation strategy presented in [29] supports both $M<1$ and $M>1$ operation mode. However, it only achieves the resonant current RMS minimization within the boundary conditions and fails to realize ZVS on the secondary-side power switches. In [9], a 3DOF optimized modulation strategy for the T-type TL converter is proposed, where the introduction of switching frequency as an additional degree of freedom enables minimization of the resonant current rms. Nevertheless, it does not achieve secondary-side ZVS, lacks closed-form analytical solution, and the frequency variation range is wide. The VFM+PSM modulation strategy in [8] is similar with that in [9]. Although the 4DOF modulation strategy [30] considers the phase margin between voltage and current to achieve ZVS on the secondary side, meanwhile achieving the quasi-minimum RMS value of the resonant. However, this method depends heavily on numerical precomputation and does not offer closed-form analytical solutions. Moreover, its wide frequency variation range poses significant challenges for magnetic component design and power density optimization. By contrast, the proposed strategy achieves a well-balanced trade-off by providing the analytical control expressions, realizing the full-range ZVS and quasi-minimum rms of the resonant current, and maintaining the low complexity within a narrow frequency range.

C. Loss Breakdown

To further analyze the efficiency of the proposed optimized modulation strategy, a general power loss model of the proposed converter is established. Based on this model, the detailed loss breakdown and comparison between the proposed strategy and the MCT strategy are carried out. The total power loss of the converter mainly consists of the switching loss and conduction loss of power switches, as well as the core loss and copper loss of magnetic components.

1) Switching Loss: The switching loss of MOSFET is calculated as

$$P_{sw} = f_s \begin{pmatrix} 0.5\sigma_1 V_{DC} I_{Don} t_r + 0.5\sigma_2 V_{DC} I_{Doff} t_f \\ +0.5 C_{oss} {V_{DS}}^2 + Q_g V_g + \sigma_3 Q_{rr} V_{rr} \end{pmatrix} \quad (25)$$

where f_s is the switching frequency. $V_{\rm DS}$ is the drain source voltage. $I_{\rm Don}$ and $I_{\rm Doff}$ are the turn-ON and turn-OFF drain current, respectively. t_r and t_f are the rise time and fall time. $C_{\rm oss}$ is the output capacitance. Q_g and V_g are the gate charge and gate voltage, respectively. Q_{rr} and V_{rr} are reverse recovery charge and voltage, respectively. The variables σ_1, σ_2, and σ_3 are equal to 0 or 1 according to the specific soft-switching conditions (ZVS turn-ON or ZCS turn-OFF).

The switching loss is related to MOSFET parameters and soft-switching performance. The part number of MOFSFET is IPW60R070C6. Combined with the parameters read from the MOSFET datasheet, the switching loss can be calculated.

2) Conduction Loss: The conduction loss of power switches is calculated as

$$P_{\rm cond} = R_{\rm DSon} \cdot {i_{\rm DSRMS}}^2 \tag{26}$$

where the $i_{\rm DSRMS}$ is the rms value of current. The $R_{\rm DSon}$ is the drain-source ON-state resistance of the power switches, which is known from the MOSFET datasheet.

3) Core Loss: The core loss is calculated by means of the improved Steinmetz equation. The equation is

$$P_{\rm core} = V_{\rm core} \cdot 4^{\alpha} \cdot k \cdot {f_s}^{\alpha} \cdot {B_{\rm pk}}^{\beta} \tag{27}$$

where $V_{\rm core}$ is the core volume, $B_{\rm pk}$ is defined as half of the peak ac flux density. The parameters k, α, β are constants obtained from curve fitting for a given material with relative permeability. The sendust toroid core is used as the magnetic coupling core in this article. The related parameters and *B-H* curve are obtained from the datasheet. Then, the core loss can be calculated.

4) Copper Loss: The copper loss generated in the inductor windings and in the transformer windings are calculated as

$$\begin{cases} P_{\rm copper} = P_{\rm copper,Tr} + P_{\rm copper,Lr} \\ P_{\rm copper,Tr} = R_L(f_s) \cdot {i_{r,\rm RMS}}^2 \\ P_{\rm copper,Lr} = R_{\rm Tr}(f_s) \cdot {i_{r,\rm RMS}}^2 \end{cases} \tag{28}$$

where R_L (f_s) and $R_{\rm Tr}(f_s)$ are the copper resistance of the inductor and transformers at the switching frequency, respectively. $i_{\rm LRMS}$ is the rms value of the current flowing through them.

5) Total Loss: In the general power loss model, the cooling loss and the fixed loss of the drive circuit is not discussed. Total loss $P_{\rm all,loss}$ is calculated as

$$P_{\rm all,loss} = P_{\rm sw} + P_{\rm cond} + P_{\rm core} + P_{\rm cu}. \tag{29}$$

Based on the above-mentioned analysis, a comprehensive estimation of the total energy loss is presented in (25)–(29). Each loss component is quantitatively evaluated based on device parameters, magnetic core characteristics, and the rms values of the current. In order to evaluate the loss breakdown, Bar chart of loss distribution between the proposed modulation strategy and MCT modulation strategy under the different transfer power is drawn in Fig. 24. As shown in Fig. 24, under the low transfer power conditions, the conduction loss and copper loss of magnetic components in the proposed modulation strategy are comparable to those of the MCT strategy. However, the proposed strategy achieves ZVS of all power switches and switching losses are lower than the MCT strategy. As the transfer power increases, the proposed strategy exhibits the lower conduction loss and copper loss compared to the MCT strategy, while the switching losses of both remain approximate. Therefore, it is seen that the proposed modulation strategy achieves lower or equal switching loss, conduction loss, and copper loss across different power levels, thereby reducing the power loss and improving the system efficiency.

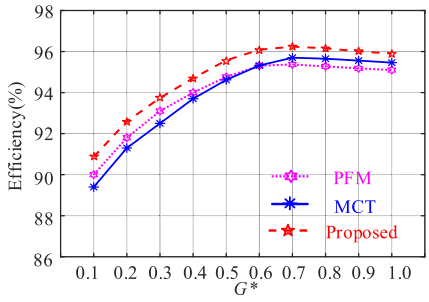

Fig. 25. Efficiency curves of proposed converter under different modulation strategies.

Finally, by using the same proposed topology, the efficiency of the proposed converter in the forward mode is tested under the MCT modulation strategy, the PFM modulation strategy and the proposed modulation strategy. The efficiency curves at the different power levels are shown in Fig. 25. Under the proposed modulation strategy, the efficiency exceeds 90% across the entire power range, with the peak efficiency reaching 96.3%. Compared to the MCT and PFM modulation strategy, the full range ZVS of the power switches and the quasi-minimum rms value of the high-frequency resonant current are achieved simultaneously under the proposed optimization modulation strategy. Therefore, the current stress, switching loss, and conducting losses are decreased. Throughout the entire power range, the efficiency under the proposed modulation strategy is higher than those under the MCT and PFM modulation strategies.

V. Conclusion

In this article, a bidirectional isolated HBTL resonant dc–dc converter is proposed. The symmetric four-switch TL structure and the compact design are used without the clamping diodes, power switches, or flying capacitors in the proposed converter features. The system volume and cost are reduced. Under the proposed full-range ZVS optimization modulation strategy based on the QMCT, the full-range ZVS of the power switches is achieved, meanwhile the quasi-minimum rms value of the high-frequency resonant current is realized in the entire power. Therefore, the current stress, switching loss, and conducting losses are reduced and the efficiency of the proposed converter is improved. Moreover, the proposed modulation strategy is universal and applied to other types of resonant dc–dc converters.

References

[1] G. Xu, W. Qiu, Y. Liu, W. Xiong, and M. Su, "Modified voltage matching control and inductor current injections for hybrid-bridge-based DAB converter," *IEEE Trans. Ind. Electron.*, vol. 70, no. 10, pp. 10227–10238, Oct. 2023.

[2] P. Shan, Y. Sun, Y. Song, F. Zhang, Y. Li, and K. Sun, "Adaptive parameter tuning and virtual impedance injection control for coupled harmonic mitigation of photovoltaic converter," *IEEE Trans. Power Electron.*, vol. 40, no. 1,pp. 162–175, Jan. 2025.
[3] H. Wu, K. Sun, Y. Li, and Y. Xing, "Fixed-frequency PWM-controlled bidirectional current-fed soft-switching series-resonant converter for energy storage applications," *IEEE Trans. Ind. Electron.*, vol. 64, no. 8, pp. 6190–6201, Aug. 2017.
[4] T. Zhu, F. Zhuo, F. Zhao, F. Wang, H. Yi, and T. Zhao, "Optimization of extended phase-shift control for full-bridge CLLC resonant converter with improved light-load efficiency," *IEEE Trans. Power Electron.*, vol. 35, no. 10, pp. 11129–11142, Oct. 2020.
[5] X. Li et al., "Data-driven modeling with experimental augmentation for the modulation strategy of the dual-active-bridge converter," *IEEE Trans. Ind. Electron.*, vol. 71, no. 3, pp. 2626–2637, Mar. 2024.
[6] S. A. Gorji, H. G. Sahebi, M. Ektesabi, and A. B. Rad, "Topologies and control schemes of bidirectional DC–DC power converters: An overview," *IEEE Access*, vol. 7, pp. 117997–118019, 2019.
[7] D. Mou et al., "Overview of multi-degree-of-freedom modulation techniques for dual active bridge converter," *IEEE J. Emerg. Sel. Top. Power Electron.*, vol. 11, no. 6, pp. 5724–5737, Dec. 2023.
[8] Y. Xuan, X. Yang, W. Chen, T. Liu, and X. Hao, "A novel three-level CLLC resonant DC-DC converter for bidirectional EV charger in DC microgrids," *IEEE Trans. Ind. Electron.*, vol. 68, no. 3, pp. 2334–2344, Mar. 2021.
[9] K. Kalayci, O. Demirel, U. Arifoglu, and H. Hizarci, "Analysis of three-level T-type LLC resonant isolated bidirectional DC-DC converter under three-degrees-of-freedom modulation," *IEEE Access*, vol. 11, pp. 60605–60625, 2023.
[10] Q. Gu, L. Yuan, S. Yi, J. Nie, and Z. Zhao, "Active selection of current commutation loop for hybrid three-level dual active bridge DC-DC converter with TPS control," in *Proc. IEEE 10th Int. Symp. Power Electron. Distrib. Gener. Syst.*, 2019, pp. 155–161.
[11] Z. Zhang et al., "Optimized modulation strategy of NH3L-DAB converter to minimize RMS current for wide voltage range applications," *IEEE Trans. Power Electron.*, vol. 37, no. 7, pp. 7789–7808, Jul. 2022.
[12] P. Liu, C. Chen, and S. Duan, "An optimized modulation strategy for the three-level DAB converter with five control degrees of freedom," *IEEE Trans. Ind. Electron.*, vol. 67, no. 1, pp. 254–264, Jan. 2020.
[13] G. Yang, F. Xiao, X. Fan, R. Wang, and J. Liu, "Three-phase three-level phase-shifted PWM DC–DC converter for electric ship MVDC application," *IEEE J. Emerg. Sel. Top. Power Electron.*, vol. 5, no. 1, pp. 162–170, Mar. 2017.
[14] H. Higa and J. Itoh, "Derivation of operation mode for flying capacitor topology applied to three-level DAB converter," in *Proc. IEEE 2nd Int. Future Energy Electron. Conf.*, 2015, pp. 1–6.
[15] Z. Guo and K. Sun, "Three-level bidirectional DC–DC converter with an auxiliary inductor in adaptive working mode for full-operation zero-voltage switching," *IEEE Trans. Power Electron.*, vol. 33, no. 10, pp. 8537–8552, Oct. 2018.
[16] H. -Y. Yueh, J. -Y. Lin, H. -J. Chiu, C. -Y. Chu, Y. -C. Chang, and S. -Y. Lee, "Three-level Bi-directional half-bridge CLLC resonant converter for DC micro-grid," in *Proc. 10th Int. Conf. Power Electron. ECCE Asia*, 2019, pp. 1904–1909.
[17] L. Jin, B. Liu, and S. Duan, "ZVS soft switching operation range analysis of three-level dual-active bridge DC–DC converter under phase Shift control strategy," *IEEE Trans. Ind. Appl.*, vol. 55, no. 2, pp. 1963–1972, Mar./Apr. 2019.
[18] P. Liu, C. Chen, S. Duan, and W. Zhu, "Dual phase-shifted modulation strategy for the three-level Dual active bridge DC–DC converter," *IEEE Trans. Ind. Electron.*, vol. 64, no. 10, pp. 7819–7830, Oct. 2017.
[19] A. Filba-Martinez, S. Busquets-Monge, J. Nicolas-Apruzzese, and J. Bordonau, "Operating principle and performance optimization of a three-level NPC dual-active-bridge DC-DC converter," *IEEE Trans. Ind. Electron.*, vol. 63, no. 2, pp. 678–690, Feb. 2016.
[20] Q. -X. Guan, Y. Zhang, H. -B. Zhao, and Y. Kang, "Optimized switching strategy for ANPC–DAB converter through multiple zero states," *IEEE Trans. Power Electron.*, vol. 37, no. 3, pp. 2885–2898, Mar. 2022.
[21] J. Tian, C. Zhuo, F. Wang, and H. Deng, "An RMS current minimization method for three-level ANPC-DAB-based distributed energy storage system with full operation ZVS," *IEEE J. Emerg. Sel. Top. Power Electron.*, vol. 12, no. 3, pp. 2388–2405, Jun. 2024.
[22] I. Barbi, R. Gules, R. Redl, and N. O. Sokal, "DC-DC converter: Four switches V/sub pk/= V/sub in//2, capacitive turn-off snubbing, ZV turn-on," *IEEE Trans. Power Electron.*, vol. 19, no. 4, pp. 918–927, Jul. 2004.
[23] D. Liu, F. Deng, Q. Zhang, and Z. Chen, "Zero-voltage switching PWM strategy based capacitor current-balancing control for half-bridge three-level DC/DC converter," *IEEE Trans. Power Electron.*, vol. 33, no. 1, pp. 357–369, Jan. 2018.
[24] W. Liu, H. Jin, W. Yao, and Z. Lu, "An interleaved PWM method with better voltage-balancing ability for half-bridge three-level DC/DC converter," *IEEE Trans. Power Electron.*, vol. 33, no. 6, pp. 4594–4598, Jun. 2018.
[25] Y. Shi, X. Wang, J. Xi, X. Gui, and X. Yang, "Wide load range ZVZCS three-level DC–DC converter with compact structure," *IEEE Trans. Power Electron.*, vol. 34, no. 6, pp. 5032–5037, Jun. 2019.
[26] J. L. S. Geraldis, C. B. Nascimento, and E. Agostini, "Improved isolated four-switch three-level soft-switching half-bridge DC-DC converter," *IEEE Trans. Power Electron.*, vol. 39, no. 4, pp. 4301–4312, Apr. 2024.
[27] D. Yang et al., "High-efficiency bidirectional three-level series-resonant converter with buck-boost capacity for High-output voltage applications," *IEEE Trans. Transp. Electrific.*, vol. 7, no. 3, pp. 969–982, Sep. 2021.
[28] L. Corradini, D. Seltzer, D. Bloomquist, R. Zane, D. Maksimović, and B. Jacobson, "Minimum current operation of bidirectional dual-bridge series resonant DC/DC converters," *IEEE Trans. Power Electron.*, vol. 27, no. 7, pp. 3266–3276, Jul. 2012.
[29] F. Wu, K. Wang, and S. Luo, "Hybrid-three-level current-fed series-resonant isolated DC-DC converter and its optimization modulation strategy," *IEEE Trans. Power Electron.*, vol. 37, no. 1, pp. 196–205, Jan. 2022.
[30] M. Yaqoob, K. H. Loo, and Y. M. Lai, "A four-degrees-of-freedom modulation strategy for dual-active-bridge series-resonant converter designed for total loss minimization," *IEEE Trans. Power Electron.*, vol. 34, no. 2, pp. 1065–1081, Feb. 2019.

Guangfu Hu received the B.S. and M.S. degrees in electrical engineering, in 2021 and 2023, respectively, from Harbin Institute of Technology (HIT), Harbin, China, where he is currently working toward the Ph.D. degree in electrical engineering.

His research interests include dc/dc power conversion and grid-connected power conversion for new energy systems.

Fengjiang Wu (Senior Member, IEEE) received the B.S., M.S., and Ph.D. degrees in electrical engineering from the Harbin Institute of Technology (HIT), Harbin, China, in 2002, 2004, and 2007, respectively.

Since 2007, he has been with the Department of Electrical Engineering, HIT, where he is currently a full Professor. He has authored or coauthored more than 100 top-tier journal articles. His research interests include the area of renewable energy generation, solid-state transformers, and microgrids.

Dr. Wu serves as an Associate Editor for IEEE ACCESS and IET POWER ELECTRONICS.

Yongfeng Qin received the B.S. degree in electrical engineering, in 2023, from Harbin Institute of Technology (HIT), Harbin, China, where he is currently working toward the Master's degree.

His current research interests include physics-informed machine learning, converter parameter identification, and remaining useful life prediction.